ACS OMEGA

http://pubs.acs.org/journal/acsodf

Article

Magnesium Bismuth Ferrite Nitrogen-Doped Carbon Nanomagnetic Perovskite: Synthesis and Characterization as a High-Performance Electrode in a Supercapacitor for Energy Storage

Basheer Mohammed Al-Maswari,* Nabil Al-Zaqri, Khaled Alkanad, Fares Hezam AlOstoot, Ahmed Boshaala, Rayapura Thimmegowda Radhika, and Bellale Marigowda Venkatesha*

Cite This: *ACS Omega* 2023, 8, 16145−16157

Read Online

ABSTRACT: Bismuth ferrite ($BiFeO_3$) is regarded as an important ABO_3 perovskite in the areas of energy storage and electronics. A high-performance novel $MgBiFeO_3$-NC nanomagnetic composite (MBFO-NC) electrode was prepared using a perovskite ABO_3-inspired method as a supercapacitor for energy storage. The electrochemical behavior of the perovskite $BiFeO_3$ has been enhanced by magnesium ion doping in the basic aquatic electrolyte as the A-site. H_2-TPR revealed that the doping of Mg^{2+} ions at the Bi^{3+} sites minimizes the oxygen vacancy content and improves the electrochemical characteristics of $MgBiFeO_3$-NC. Various techniques were used to confirm the phase, structure, surface, and magnetic properties of the MBFO-NC electrode. The prepared sample showed an enhanced mantic performance and specific area with an average nanoparticle size of ∼15 nm. The electrochemical behavior of the three-electrode system was shown by cyclic voltammetry to have a significant specific capacity of 2079.44 F/g at 30 mV/s in 5 M KOH electrolyte. GCD analysis at a 5 A/g current density also showed an enhanced capacity improvement of 2159.88 F/g, which is 3.4× higher than that of pristine $BiFeO_3$. At the power density of 5284.83 W/kg, the constructed MBFO-NC//MBFO-NC symmetric cell showed an exceptional energy density of 730.04 W h/kg. The MBFO-NC//MBFO-NC symmetric cell was employed as a direct practical application of the electrode material to entirely brighten the laboratory panel, which had 31 LEDs. This work proposes the utilization of duplicate cell electrodes made of MBFO-NC//MBFO-NC in portable devices for daily use.

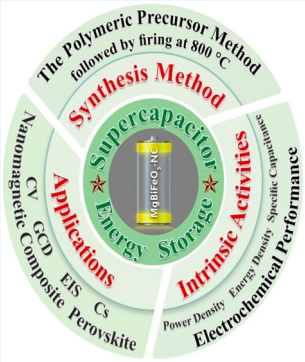

1. INTRODUCTION

With the world's increasing population and the current energy crisis, fears regarding the generation and use of electrical power have arisen. As a consequence, a potential alternative energy storage technology other than what is now available is needed. Batteries are the most extensively used and preferred alternatives due to their high energy capacity and low voltage supply. Capacitors, as a result, remain the most effective devices for storing massive loads of energy at high power levels. Nanostructures have distinct physical and chemical features that make them an attractive choice for wide applications in industries such as supercapacitors, electronics, and energy storage devices. It should be clear that energy storage is a crucial tool for meeting the world's growing demand for energy generation and consumption.[1] The energy storage and conversion properties of perovskite-type (ABX_3) materials are particularly advantageous among others nanoheterostructures. Moreover, in regard to fossil fuel depletion and climate change, much attention has been invested in offering innovative renewable energy storage systems.[2] The hunt for affordable, highly effective electrode materials for use in upcoming energy applications is a research hotspot. Supercapacitors are a relatively recent kind of electrochemical energy storage device. They operate on a similar concept as rechargeable batteries in terms of how they store charge rather than electrostatic capacitors. Due to their exceptional performance qualities, these devices can be utilized to meet needs for long-term electrical energy storage. Scientists have researched the relationship between the magnetic, electric, and ferroelectric characteristics of transition metal oxides to develop switchable multifunctional nanoelectronics, magnetoelectric memory with random access, and many types of optical-electronic devices.[3]

Ferromagnetic materials are materials that are strongly attracted to an external magnetic field. This type of material has more unpaired electrons in its metal atoms or metal ions. Thus, any excitation of the ferromagnetic material causes a transfer of individual electrons. This transfer increases the electrical conductivity (electrochemical), greatly benefiting supercapacitors and energy storage devices. Similarly, a

Received: January 13, 2023
Accepted: April 18, 2023
Published: May 1, 2023

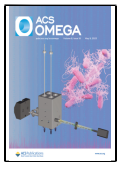

https://doi.org/10.1021/acsomega.3c00259
ACS Omega 2023, 8, 16145−16157

ferroelectric material has spontaneous electric polarization. The reversing of the polarity of a ferroelectric material through applying an external electric field is known as switching behavior.[4] Ferroelectric materials can also maintain polarization after the removal of the electric field. The relationship between the ferroelectric and ferromagnetic materials is that they have similarities in polarization. Ferroelectric materials have many applications, and supercapacitors are one of them.[5] In addition, electricity and magnets are two sides of the same coin according to the laws of electromagnetism. An electric current can create a magnetic field. Conversely, a changing magnetic field can create an electric current in a physical phenomenon called electromagnetic induction. Perovskite $BiFeO_3$ (BFO) of a single-phase multiferroic material has received the most attention, as it exhibits a high link between the magnetism in the ground state and the random electric polarization.[3] At low temperatures, BFO goes through two phase transitions: one from paraelectric to ferroelectric at temperatures around 830 °C and another from paraelectric to magnetoelectric at 370 °C (Néel temperature). The stereochemical activity of the Bi^{3+} $6s^2$ lone electronic pair controls the ferroelectric mechanism for $BiFeO_3$, which is responsible for transferring charge from the $6s^2$ orbital to nominally empty 6p orbitals, while the residue momentum from the cantilevered Fe^{3+} spin structure is responsible for the weak ferromagnetic feature.[6] The interaction influence between electric and magnetic properties generated by $BiFeO_3$ lattice distortion has highlighted the various techniques to integrate magnetism and ferroelectricity in multiferroic materials. New studies on improving the magnetic and electrical characteristics of the thin film $BiFeO_3$ have revealed that the addition of common A-site dopants like M^{+2} can significantly reduce $BiFeO_3$'s current leakage. The leakage current and aging concerns of $BiFeO_3$ films are both linked to oxygen vacancies, and lowering the oxygen vacabct concentration is a good strategy to alleviate both problems at the same time. However, the number of oxygen vacancies in the perovskites is crucial, which could positively enhance or negatively affect the electrochemical properties.[7] Oxygen vacancies in perovskites are considered as charge storage sites for pseudocapacitance.[7c] Hence, the energy densities of perovskite supercapacitors could be maximized by increasing the number of oxygen vacancies. On other hand, their access could negatively affect the electrochemical properties.[7a] Doping Mg^{2+} ions at the Bi^{3+} site is an effective technique to minimize the oxygen vacancy content and improve the characteristics of $BiFeO_3$. The doping quantity can control the ferroelectric and ferromagnetic characteristics, allowing for unique multifunctional applications.[8] The antiferromagnetic structure in $BiFeO_3$ involves a complex interaction of interchange and spin−orbit pairing that influences Fe ions. Chemical alterations, morphology, and structure control are all options for improving the magnetic properties. In terms of morphologies, $BiFeO_3$-based nanostructures demonstrate higher magnetization than comparable bulks because of the specific size of nanoparticles distributed in helimagnetic order.[9]

Another strategy to change the magnetic structure is to replace Bi with Mg^{2+} ions because the super exchange interaction between localized Mg 2p and Fe 3d electrons may be significant in the perovskite-like structure. Activated carbon is the most well-known active component used to make electric double-layer capacitor (EDLC) electrodes. Additional improvements to this carbon material are necessary to make the activated carbon electrodes compatible with electrolytes.[10] Due to of its unique qualities, such as reasonably high electronic conductivity, low price, and adequate chemical stability, activated carbon is preferable.[10b] Therefore, the electrolyte and electrode surface ions form a double layer. This is a crucial characteristic of an energy device, especially EDLC, which can retain more energy, so it is possible to use a non-Faradaic technique to store charge in an EDLC. This can be further explained by claiming that ions from the electrolyte compensate for the charge on the electrodes' electrons by shifting in that direction.[11] In contrast, an EDLC outperforms Faradaic capacitors or pseudocapacitors in terms of comparably higher stability, power density, thermal stability, greater reversibility, safety, cost-effectiveness, and simpler fabrication methods.[12] Moreover, nitrogen molecules present a number of interpreting obstacles in the fields of structural chemistry, energy conversion, electronics, physical chemistry, materials chemistry, biochemistry, and energy storage because of their high electronegativity, small size, high ionization enthalpy, and absence of a d orbital.[13] It is very interesting to see how N interacts with the local atomic coordination structure and the importance of these coordination structures for the local structure and conductivity performance.[14]

Recent studies have shown that heteroatom N doping in a carbon matrix is capable of generating polar covalent bonds between the nitrogen and carbon atoms due to their similar atomic sizes.[15] Furthermore, the C−C bond is weaker than the C−N bond because the C and N atoms have a higher rate of charge buildup.[16] Remarkably, a reasonable quantity of nitrogen doping results in various local structures, which are advantageous for increasing (Cs) the electrical conductivity.[16a] Electrocatalytic reactions also have the potential to alter the adsorption behavior of oxygen and hydrogen atoms. In this study, we prepared a nanomagnetic perovskite magnesium-doped bismuth ferrite nitrogen-doped carbon (MBFO-NC MNP). The perovskite was doped with 5% magnesium versus 95% bismuth increased the magnetic and electrical properties. In addition, urea and formaldehyde were used in the polymerization process as sources of nitrogen, carbon, and oxygen, resulting in a composite with a wide surface area and enhanced magnetic properties. These make it an excellent material for electrodes, and the material has a high specific capacitance as a supercapacitor.

2. EXPERIMENTAL SECTION

2.1. Materials. The chemical reagents listed as followsare Sigma-Aldrich grade and were utilized as received: sodium hydroxide (NaOH), urea, formaldehyde, bismuth chloride ($BiCl_3$), magnesium chloride hexahydrate ($MgCl_2{\cdot}6H_2O$), and ferric chloride ($FeCl_3$).

2.2. Fabrication of the Precursors (MgBiFe-UF) and ($MgBiFeO_3$-NC). The polymerization technique was used to produce the precursors (MgBiFe-UF) for the preparation of the $MgBiFeO_3$-NC. Typically, 15 mL of formaldehyde and 6.0 g of urea were mixed at pH 7−10 using aqueous NaOH. The mixture was placed at 70 °C on a magnetic stirrer for 1 h in order to form a urea−formaldehyde (UF) polymer ligand. Later, 1.62, 3.15, and 0.1 g of $FeCl_3$, $BiCl_3$, and $MgCl_2.6H_2O$, respectively (1:0.95:0.05) ($Fe^{+3}/Bi^{+3}/Mg^{+2}$) were thoroughly mixed in 20 mL of double distilled H_2O. Finally, the dissolved mixture salts were mixed with the viscous solution (UF) of urea formaldehyde and stirred for 4 h at 70 °C, producing a three-metal polymeric precursor MgBiFe-UF. The obtained

https://doi.org/10.1021/acsomega.3c00259
ACS Omega 2023, 8, 16145−16157

MgBiFe-UF was washed thoroughly several times with double distilled H_2O and ethanol and dried at 50 °C. MgBiFe-UF precursors were then calcinated at 800 °C (5 °C per min) for 6 h in an argon atmosphere to produce the $MgBiFeO_3$-NC nanomagnetic composite. Scheme 1 shows how to prepare the target material.

Scheme 1. Polymeric Precursor Technique for the Preparation of the $MgBiFeO_3$-NC Nanomagnetic Composite

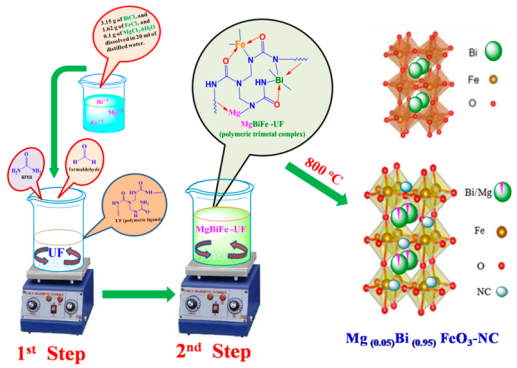

2.3. Characterization Techniques. SII 6300 EXSTAR with a reaction temperature of 10 °C/min was used to perform the thermogravimetric analysis (TGA) and the differential thermal analysis (DTA) of the fabricated $MgBiFeO_3$-NC nanomagnetic composite. Infrared (FTIR) spectra between 400 and 4000 cm^{-1} were obtained using a Bruker Tensor II instrument. The surface area for the MBFO-NC nanomagnetic composite (N_2 adsorption/desorption) was calculated using a BET Micromeritics Tristar II Plus analyzer. The oxidation states of the elements were investigated via XPS examination using a PHI 5000 Versa Probe III instrument. An X-ray diffractometer (Rigaku; λ = 1.54059 Å, Cu−K radiation) was employed to confirm the crystalline phase of sintered MBFO-NC nanomagnetic composite. Field emission scanning electron (FE-SEM) microscopy (JSM-7600F) and high-resolution transmission electron microscopy (HR-TEM) (Tecnai G2, F30) were used to determine the morphology of the MBFO-NC nanomagnetic composite.

2.4. Electrochemical Studies. The electrochemical property of the prepared $MgBiFeO_3$-NC nanomagnetic composite was tested using an electrochemical workstation (CHI 608e) with a three-electrode system. 3 mg of the MBFO-NC nanomagnetic composite was dispersed in 2 mL of isopropanol containing 0.004 mL of a Nafion solution. Prior to the experimentation, argon gas was purged for 30 min. A small amount of the suspension solution, approximately 0.18 mg/cm^2, was dropped on the glassy carbon electrode (working electrode) and dried in the vacuum oven at 50 °C. Platinum

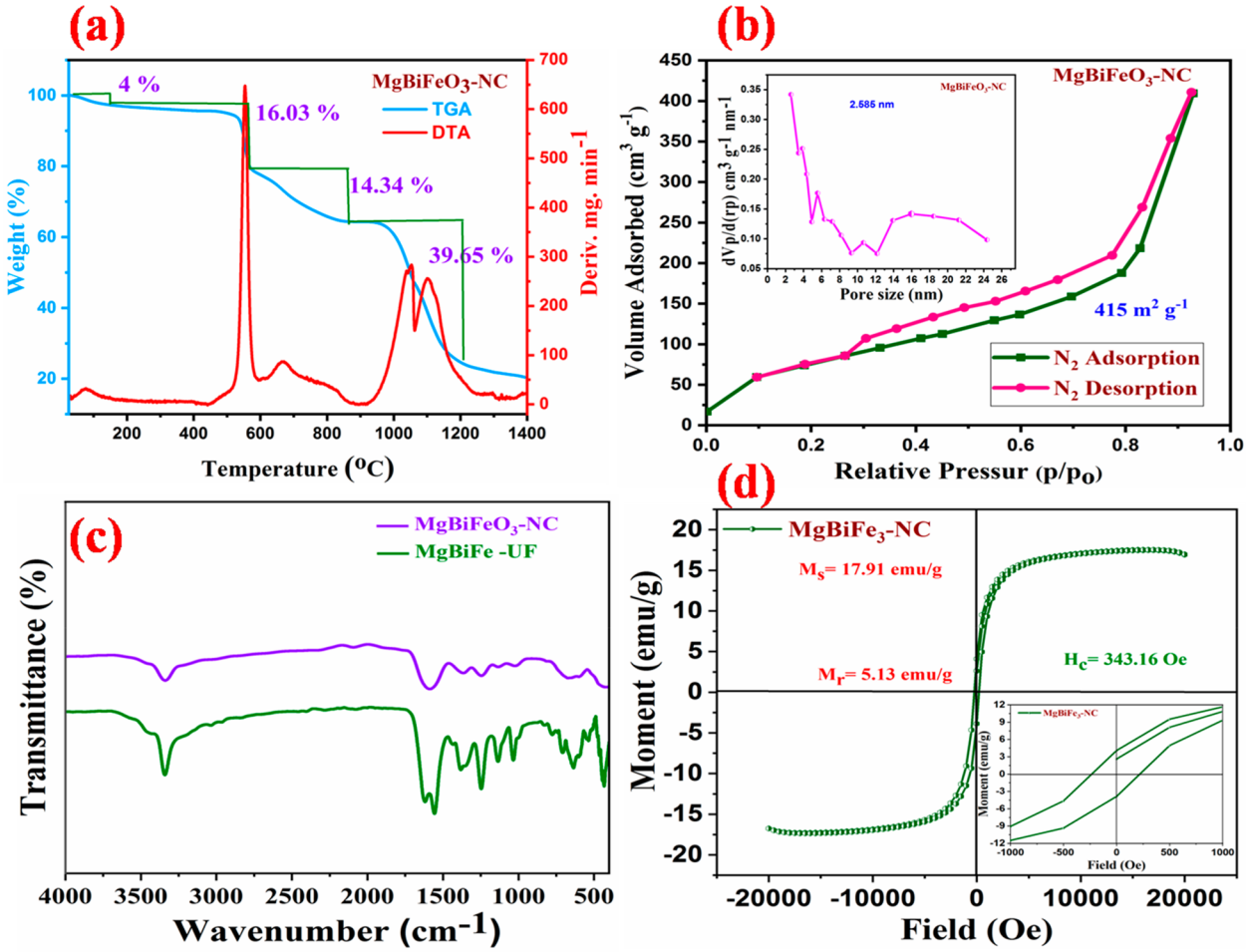

Figure 1. (a) Thermal analysis of the MBFO-NC, (b) BET surface area of the MBFO-NC, (c) FT-IR bands of MgBiFe-UF and $MgBiFeO_3$-NC, and (d) VSM curve of MBFO-NC.

https://doi.org/10.1021/acsomega.3c00259
ACS Omega 2023, 8, 16145−16157

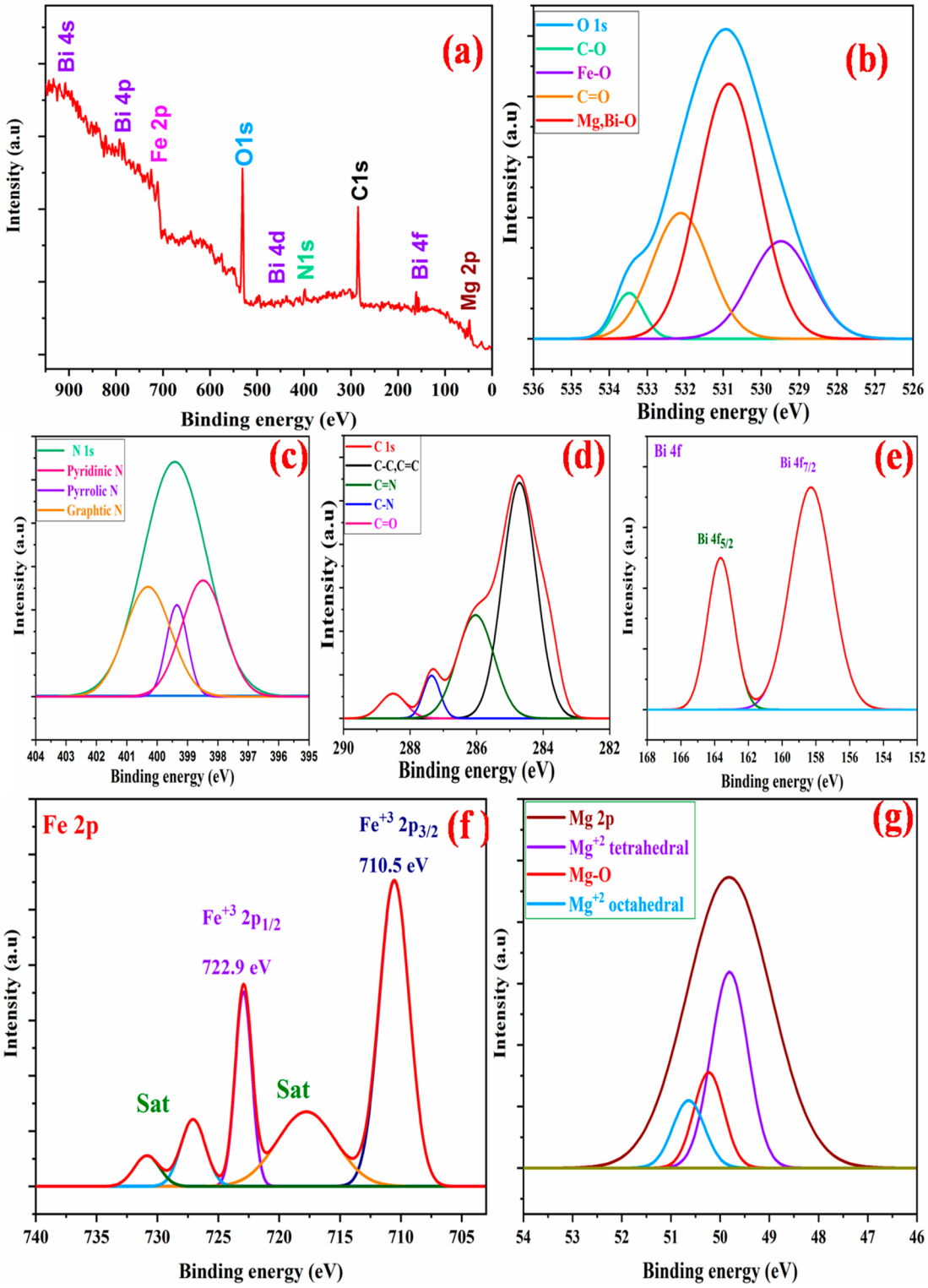

Figure 2. XPS spectrum of the MBFO-NC: (a) comprehensive survey of $MgBiFeO_3$-NC, (b) O 1s spectra, (c) N 1s spectra, (d) C 1s spectra, (e) Bi 4f spectra, (f) Fe 2p spectra, and (g) Mg 2p spectra.

wire, KOH (5M), and Ag/AgCl were utilized as a counter electrode, an electrolyte, and a reference electrode, respectively. Galvanic charge−discharge (GCD), cyclic voltammetry (CV), and electrochemical impedance spectroscopy (EIS) were performed. The EIS testing was done in an open circuit using an AC voltage with 5 mV amplitude and frequencies between 10 kHz and 0.1 MHz.

3. RESULTS AND DISCUSSION

A three-region collapse pattern was seen in the TGA curve for MBFO-NC, as shown in Figure 1a. In the first stage, 4% of the MBFO-NC weight loss of humidity occurred in the region between 25 and 140 °C. The second phase is mass decrease due to the oxidative decomposition of organic matter weight loss of 16.03% at 140−570 °C. There were mass losses of

https://doi.org/10.1021/acsomega.3c00259
ACS Omega 2023, 8, 16145−16157

14.34% and 39.65% in the third and fourth thermal transitions, respectively, between 570 and 1200 °C due to the thermal collapse of carbon and related small organic compounds. As expected, three peaks appear in the DTA curve, and this suggests that the method in which the MBFO-NC nanomagnetic compound was synthesized was accompanied by an exothermic process. The peak at 555 °C represents the disintegration of the gel phase and the loss of organic mass. At 1047 and 1105 °C, the antiferromagnetic material turns paramagnetic, exceeding the Neel temperature of MBFO-NC.[16c,17] The BET surface area and porosity of the MBFO-NC nanomagnetic composite were determined. Figure 1b shows that MBFO-NC nanomagnetic composite has a high surface area of around 415 m^2/g. The BET curve reveals that MBFO-NC nanomagnetic composite is type IV. Using the BJH model, it was estimated that the mean pore size distribution is 2.585 nm (Figure 1b). A material with a large pore size distribution and surface area enhances electrochemical performance.[18] The porosity curve shows narrower peaks indicating mesoporous structural homogeneity. The existence of many pyramidal pores linked by sinuous, long corridor channels would aid in the retention and accessibility of electrolytes inside the carbon matrix. The presence of two important factors increases the capacities of the electrochemical energy storage rate; the first is the large surface area, which contributes to a higher surface density active sites, and the second is the mesoporous structures, which allow the transfer of electrolyte ions with high efficiency.[16c,19]

The fabricated MgBiFe-UF precursor and $MgBiFeO_3$-NC nanomagnetic composite have been studied using FT-IR spectroscopy (Figure 1c). Many bands have appeared, namely O−H/N−H and C−H stretching, C−N, C═O, C−H bending, C−O−Fe, C−C, C−O−Bi/−O−Mg, and C−O bonds, due to the prominent vibration bands of the present functional groups in the FT-IR spectra of MgBiFe-UF at 3404−3274, 2982−2918, 1565, 1620, 1405, 1349, 1247, 1139.84, and 1035.68 cm^{-1}, respectively. In addition, FT-IR bands of Fe/Bi−N, Mg−O, Bi−O, and Fe−O appeared at 451−443, 532.87, 639.5, and 764 cm^{-1}, respectively. The two IR bands demonstrated the perovskite structure's octahedral shape at ∼580 and ∼442 cm^{-1}. These bands appeared due to Fe−O bond bending vibrations in $[FeO_6]$ and $[BiO_6]$ octahedra. Owing to the Fe−O bending vibration and the Bi−O expansion vibration of these groups, the Bi−O bond vibration may cause a wide peak of ∼1018 cm^{-1}.[20] The decomposition of MgBiFe-UF into the $MgBiFeO_3$-NC nanocomposite resulted in the disappearance of some FTIR bands. As illustrated in Figure 1d, the magnetic properties of MBFO-NC nanomagnetic composite were investigated using vibrating-sample magnetometry (VSM) under a 5 T applied magnetic field at 300 K to determine values (H_C, M_R, and M_S). The temperature has a substantial influence on the saturation magnetization, i.e., as temperature rises, magnetization decreases. As the temperature rises, the magnetic moments of nanoparticles distort and the anisotropic constant decreases.[29] Both effects at higher temperatures contribute to lower magnetization.[21] Although the external magnetic field has an effect on the domain walls of hard magnetic materials, the field walls do not change significantly. Furthermore, particle size and chemical composition influence the structure and size of a ferrite's compound hysteresis loop.[21] High saturation magnetization and coercivity are found in single-domain ultrafine powders.[22] When the size of the particle is smaller than the critical size, the creation of domain walls is hampered, resulting in a single domain structure and uniformly magnetized nanoparticles. In order to assess the particle size, the magnetic domain rotation is used as the size of the particle reaches near its critical value, and the coercivity (H_C) attains its highest value. As the particle size approaches critical size, high magnetism causes the coercive field of single-domain particles to diminish, whereas the magnetic moment rotates freely in multidomain particles due to domain barriers; increasing particle size reduces coercivity.[23] It was observed that the sample's magnetic coercivity increases as the size of the particles decreases, indicating an inverse relationship between the two variables because the sample's magnetic coercivity is affected by factors such as particle size, crystal anisotropy, particle shape, field size, and porosity. In fields of ±20 kOe, the magnetic activity of the MBFO-NC was measured, and the results suggested that the compound MBFO-NC has superparamagnetism. The saturation magnetization value (M_s) was 17.91 emu/g, the coercivity value (H_C) was 343.16 Oe, the retentivity value (M_R) was 5.13 emu/g, and the M_R/M_S value was 0.286 at 300 K. XPS spectrum analysis was utilized to identify the primary elements that contributed to the construction of the MBFO-NC nanomagnetic composite (Figure 2a). The MBFO-NC nanomagnetic composite contained Mg, Bi, Fe, O, N, and C. Figure 2b shows the O 1s HR-XPS spectrum of $MgBiFeO_3$-NC, which demonstrates that they could be fitted and deconvoluted into four peaks. These peaks correspond to Fe−O, Mg/Bi−O, C═O, and C−O at 529.45, 530.87, 532.14, and 533.51 eV, respectively.[24] The N 1s HR-XPS spectrum is seen in Figure 2c. The surface of the MBFO-NC has been shown to include three different types of N atoms: pyridinic N, pyrrolic N, and graphitic N at 398.49, 399.35, and 400.30 eV, respectively.[16b,c] The HR-XPS spectrum of C 1s is displayed in Figure 2d. The peak was fitted and deconvoluted into four peaks. These peaks match to C═C/C−C, C═N, C−N, and C═O at the following binding energies: 284.72, 286.04, 287.35, and 288.47 eV, respectively.[16b] In Figure 2e, the HR-XPS Bi 4f spectrum exhibited two peaks, with the binding energies at 158.29 eV for the Bi $4f_{7/2}$ peak and at 163.67 eV for the Bi $4f_{5/2}$ peak for the (Bi^{3+}) ion.[24a,25] In the presence of Mg^{2+} in the $MgBiFeO_3$-NC (MBFO-NC) nanomagnetic composite sample, the Bi 4f peaks are somewhat displaced to the lowest binding energy due to the variation in electronic state values of Mg and Bi elements. Figure 2f shows the HR-XPS Fe 2p spectrum and exhibits two binding energies, one at 710.5 eV, which matches with Fe $2p_{3/2}$, and one at 722.9 eV, which matches with Fe $2p_{1/2}$. Fe is in the triple oxidation state (Fe^{3+}), indicating the interplay between spin−orbits. The satellite peaks confirms the presence of Fe^{3+} in the resultant nanocomposite.[24a] HR-XPS spectrum of the Mg 2p could be deconvoluted into three peaks consistent with different environments of Mg^{2+} ions: octahedral sites (Mg^{2+}) in the spinel structure at binding energy of 49.8 eV, Mg−O sites at a binding energy of 50.25 eV, and tetrahedral sites (Mg^{2+}) in the spinel structure at a binding energy of 50.64 eV in the MBFO-NC structure, as shown in Figure 2g.[26] At lower binding energies, a strength peak is attributed to Mg^{2+} in tetrahedral sites, while the smaller peak is due to the cations partially migrating to octahedral sites.[26,27]

The structure, crystallinity, and purity of the $MgBiFeO_3$-NC nanomagnetic composite were confirmed using PXRD (Figure 3). It was found that several peaks at 2θ values of 22.41°, 31.75°, 32.22°, 37.64°, 38.95°, 39.48°, 45.75°, 51.73°, 56.36°,

https://doi.org/10.1021/acsomega.3c00259
ACS Omega 2023, 8, 16145−16157

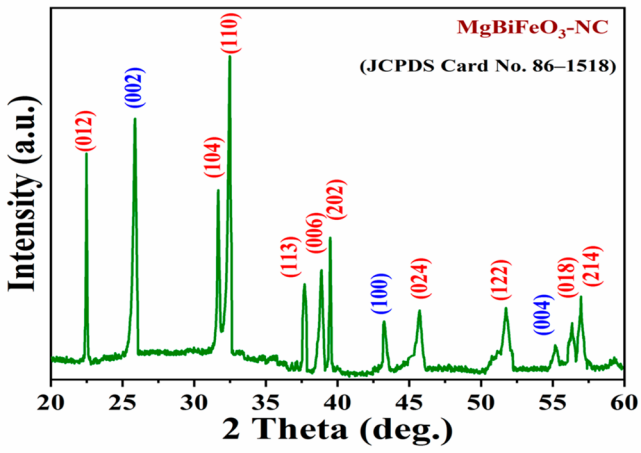

Figure 3. PXRD of the MBFO-NC nanomagnetic composite.

and 56.96° correspond to (012), (104), (110), (113), (006), (202), (024), (122), (018), and (214) miller planes, respectively. These crystal planes are attributed to the rhombohedral perovskite phase (*R*3*c*) of $BiFeO_3$ (JCPDS no.. 86-1518).[19b,24b,28] The crystal structure of $BiFeO_3$-NC (single phase *R*3*c*) would change into another phase once doped with magnesium ions.[29] This could be due to the partial transformation of the Bi−O bond into the Mg−O bond once the partial replacement of Bi^{3+} ions by Mg^{2+} ions occurred. This partial ion substitution would reduce the number oxygen vacancies in the crystal structure, improving the material's electrical conductivity.[29,30] The XRD peaks at 2θ (∼32°) reveal that when the material was doped an amount of Mg^{2+} ions, the diffraction angle shifted toward a higher angle, which also could transfer the crystal phase structure.[29] Additionally, XRD analysis confirmed the presence of N-doped graphitic carbon in the MBFO-NC nanomagnetic composite at 2θ of 25.9°, 43.2°, and 55.14° corresponding to the following miller levels: (002), (100), and (004), respectively.[16b,c,31] This confirms the success and the pureness of the fabricated nitrogen-doped carbon $MgBiFeO_3$-NC nanomagnetic composite perovskite.

Figure 4a shows the morphology of the MBFO-NC nanomagnetic composite. FE-SEM shows the fabricated composite is an establishment of spherically agglomerated nanoparticles. The annealing time (800 °C) and the magnetism attraction contributed to the aggregation of the primary ferrite nanoparticles[16b] or might be due to tiny nucleation centers clumping together to form large grains.[32] The inclusion of Mg^{2+} ions into $BiFeO_3$-NC has a significant impact on the particle size, which could indicate the phase of the nanostructured transferred to another phase with a reduced crystal unit cell volume.[29b] This fine nanometer-range particle boosts the surface area and the magnetic properties of the MBFO-NC nanomagnetic composite.[16b] Figure 4b a shows the TEM image of the MBFO-NC nanomagnetic composite, and the average particle size was found to be ∼15 nm. The HR-TEM image illustrates a prototypical crystalline area of nanoparticles in the carbon matrix.[33] Figure 4c shows the spacing lattice of 0.344 nm matches that of the (002) Miller indices of graphite carbon, suggesting the presence of carbon matrices in the MBFO-NC. The lattice spacing of 0.278 and 0.396 nm correspond to (110) and (012) Miller indices, respectively, of the rhombohedral (*R*3*c* space group)

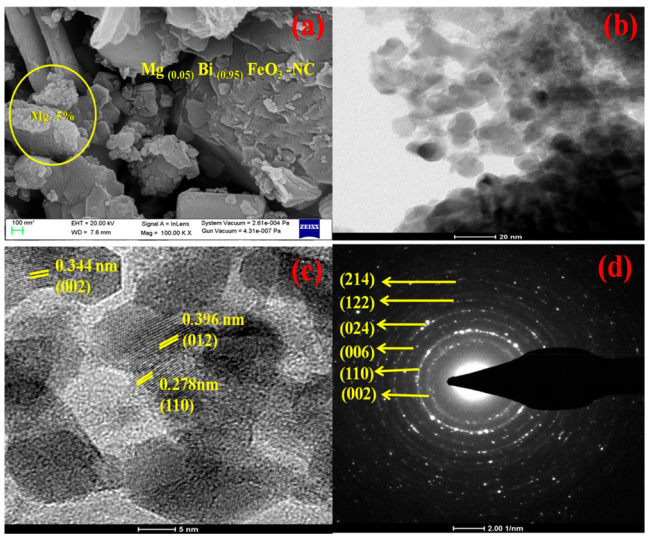

Figure 4. (a) FE-SEM, (b) TEM, and (c) HR-TEM images and (d) selected area electron diffraction (SAED) of the MBFO-NC nanomagnetic composite.

phase.[16c,28a,34] Figure 4d shows the selected area electron diffraction (SAED) of the MBFO-NC. It exhibits five intense rings indexed as (110), (006), (024), (122), and (214) of the Miller levels, which match to the rhombohedral perovskite phase (*R*3*c*) of $BiFeO_3$, where is there one ring indexed as (002) of the graphite carbon. The electron diffraction patterns of MBFO-NC demonstrate that the $BiFeO_3$ nanostructure is firmly connected with the graphite carbon. The HR-TEM and SEAD analyses closely match the XRD results (Figure 3).

Mapping images were used to confirm the distribution of elements in the $MgBiFeO_3$-NC nanomagnetic composite (Figure 5). The presence of C, O, N, Fe, Bi, and Mg components in the sample was confirmed by EDAX (Figure 5). All elements in the nanocomposite have their atomic percentages listed in the tables. The elemental composition fairly (atomic weight %) matched the stoichiometry of the elements when they were initially loaded.

Three-electrode systems were utilized to study the electrochemical properties of the MBFO-NC nanomagnetic composite. KOH (5M) was used as the electrolyte solution to determine the galvanostatic charge/discharge (GCD) and perform cyclic voltammetry (CV) and electrochemical impedance spectroscopy (EIS). CV of MBFO-NC was performed at different scan rates (30, 50, 100, 200, and 300 mV/s) and operating voltage range between −1.12 and +1.5 V. Figure 6 a shows that the CV did not exhibit any obvious redox peaks, which suggests that it resembles the approximate properties of a traditional double-layer capacitor. Bi^{3+} ions are partially replaced by Mg^{2+} ions in an attempt to reduce the oxygen vacancies, which improves the conductance of the pristine compound, as the pure $BiFeO_3$ from the perovskite structure has low electrical conductivity.[35] In the Bi site, the magnesium ions were doped into the structure $BiFeO_3$; because of the substitution of the bivalent Mg^{2+} ions for the trivalent Bi^{3+} ions, an unequal distribution of charges resulted. This demonstrates that adding heterogeneous ions to the perovskite ($BiFeO_3$) materials successfully increases their electrical conductivity. It was determined that 5% magnesium doping of $BiFeO_3$ is suitable for the replacement of Bi^{3+}. H_2−temperature-programmed reduction (H_2-TPR) analysis of the

https://doi.org/10.1021/acsomega.3c00259
ACS Omega 2023, 8, 16145−16157

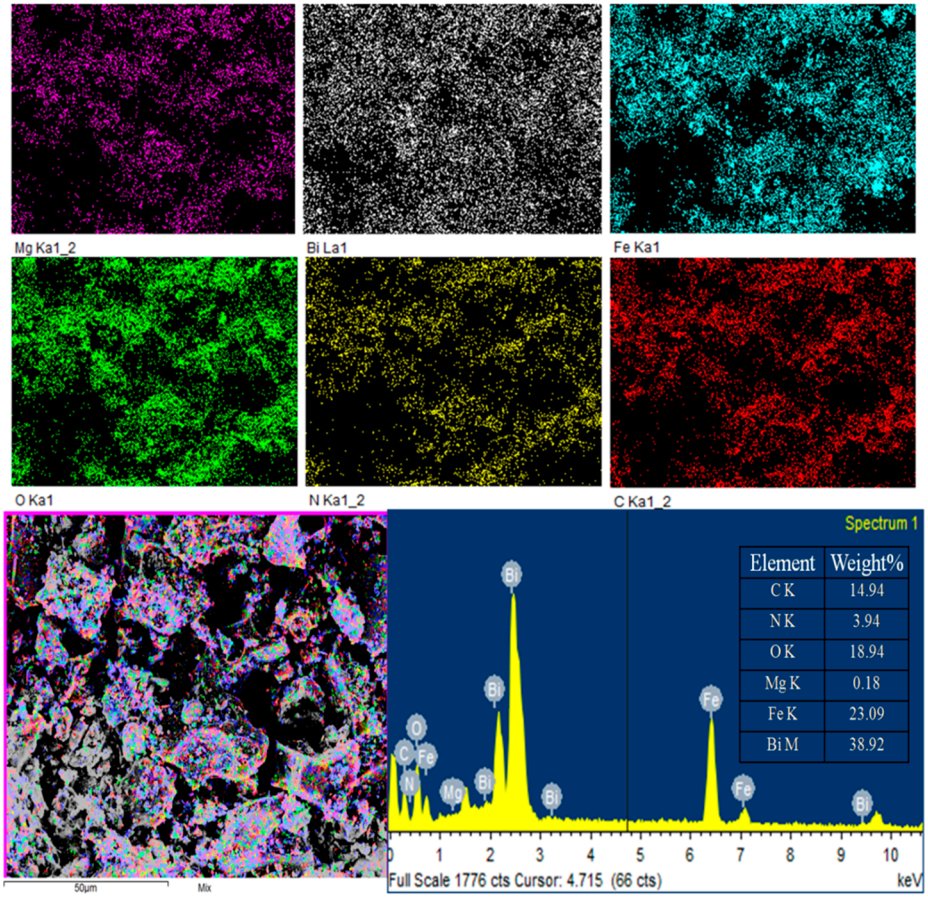

Figure 5. EDAX spectra and elemental mapping of the $MgBiFeO_3$-NC.

BFO-NC and MBFO-NC nanomagnetic composites was performed to investigate their reducibility and the presence of oxygen vacancies on the surface.[36] Figure S1 show that both samples undergo a two-step reduction at 350 and 560 °C. The low-temperature peak (350 °C) corresponds to the presence of vacancies on the surface, while the peak at a higher temperature (560 °C) indicates the lattice oxygen of the samples. It can be seen that the MBFO-NC sample has a lower intensity peak at 350 °C than the BFO-NC sample, indicating the doping of the Mg^{2+} ions at the Bi^{3+} sites reduces the oxygen vacancy availability in the $MgBiFeO_3$-NC nanomagnetic composite. As a result, CV curves found that the MBFO-NC nanocomposite has a specific capacitance (C_s) around 2079.44 F/g at 30 mV/s (Figure 6b), while pure $BiFeO_3$ shows a specific capacitance of ~613.76 F/g at 30 mV/s (Figure S2), as calculated using eq 1 as follows:

$$C_s = \frac{\int I(V)\,\mathrm{d}V}{m \times \Delta V \times v}\ \mathrm{F/g} \tag{1}$$

where $\int I(V)\,\mathrm{d}V$ symbolizes the area obtained from the CV curve, m is the active mass of the materials, ΔV is the potential window, and v is the scan rate. The values plot of C_s versus the CV curve with different scan rates is illustrated in Figure 6b. The performance of electric double-layer capacitors (EDLC) is demonstrated by the electrochemical reaction in CV (eqs 2−7). This behavior is due to the interaction of the electrode's contact with the electrolyte ions in the porous structure.

$$Bi^{3+} + 3OH^- \rightarrow Bi(OH)_3 \tag{2}$$

$$Mg^{2+} + 2OH^- \rightarrow Mg(OH)_2 \tag{3}$$

$$3Bi(OH)_3 + 3e^- \rightarrow 2BiO_2^- + 4H_2O + OH^- + Bi^{(0)} \tag{4}$$

$$2Mg(OH)_2 + 2e^- \rightarrow MgO + H_2O + 2OH^- + Mg^{(0)} \tag{5}$$

$$2Bi^{(0)} + 6OH^- \leftrightarrow Bi_2O_3 + 3H_2O + 6e^- \tag{6}$$

$$Mg^{(0)} + 2OH^- \leftrightarrow MgO + H_2O + 2e^- \tag{7}$$

Figure 6c shows the GCD studies conducted between 0−1.56 V voltages at current densities in the range of 5, 10, 20, 30, and 40 A/g. Based on GCD values of the MBFO-NC nanomagnetic composite at various current densities, eq 8 was used to calculate the C_s of the electrode in the three-electrode system.[22b,37]

$$C_s = \frac{I \times \Delta t}{m \times \Delta V}\ \mathrm{F/g} \tag{8}$$

where I and (Δt) are the discharge current and the discharge time, m is the active mass of the materials, and ΔV is the potential window. The C_s values were found to be 2159.88, 1737.11, 1241, 1005.83, and 728.22 F/g for the current densities of 5, 10, 20, 30, and 40 A/g, respectively. From the GCD studies of the MBFO-NC nanomagnetic composite, the maximum value for C_s was found to be around 2159.88 F/g at 5 A/g. With the increase of the current density from 5 to 40 A/g, the C_s values of the MBFO-NC nanomagnetic composite

https://doi.org/10.1021/acsomega.3c00259
ACS Omega 2023, 8, 16145−16157

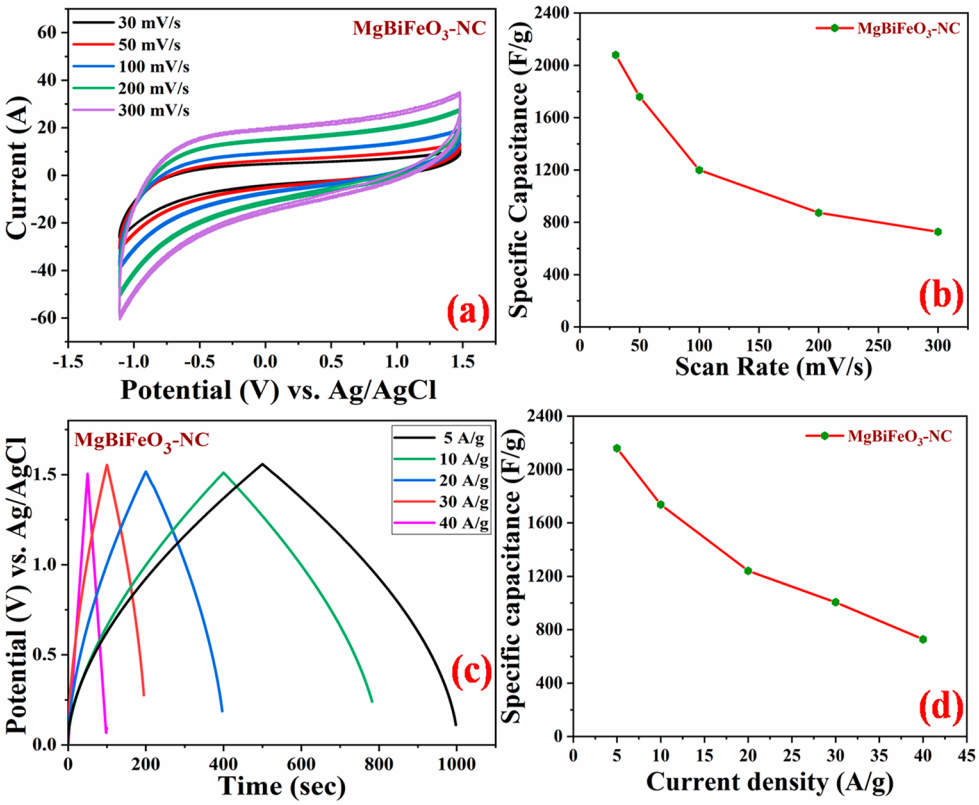

Figure 6. Electrochemical analysis of MBFO-NC nanomagnetic composite: (a) CV curvs, (b) Cs by CV plot, (c) GCD curves, and (d) Cs by GCD plot.

Table 1. Comparison of the Recent Research to Previously Reported Nanocomposites for Supercapacitors and Energy Storage

material electrode	electrolyte	scan rate (mV/s)	energy density W h/kg	power density W/kg	specific capacitance Cs (F/g)	refs
$MnFe_2O_4$/rGO	6 M KOH	5	15.9	324.5	271	44
$Ni_{1-x}Mg_xFe_2O_4$	6 M KOH	5	11.96	143.9	259.89	45
$TiO_2/BiFeO_3$	0.5 M Na_2SO_4	5	58.5	1.2	440	46
$Mg_{1-x}Zn_xFe_2O_4$	1 mol/L Na_2SO_4	5	10.8	0.5	484.6	47
rGO-$NiFe_2O_4$	1 M Na_2SO_4	5	23.7	225	210.9	48
C/Fe_3O_4	aqueous electrolyte	5	42	14500	536	49
$BiFeO_3$-NC nanocomposite perovskite	1.0 M Na_2SO_4	5			811.12	16c
$CoFe_2O_4$/graphene/PANI	6 M KOH	5	240	2680	1123	50
$SrFe_2O_4$-NC nanocomposite	5 M KOH	5	59.094	2784.977	895	22b
$BiFe_{0.95}Co_{0.05}O_3$	6 M KOH	5			278.2	51
$BiFe_{0.95}Cu_{0.05}O_3$	6 M KOH	5			568.13	52
Fe_3O_4 NAs@2DCCS	6 M KOH	5	115.5	8000	820	41
$MnTiO_3$ (MTO) perovskites	2 M KOH	5	52.2	1351.9	1513.7	53
$BiFeO_3$ -RGO	3 M KOH + 0.1 M $K_4[Fe(CN)_6]$	5	6.65	1900	928.43	54
N-CQDs/Co_3O_4 nanocomposite	6 M KOH	5	36.9	480	1867	55
MgBiFeO$_3$-NC (MBFO-NC) nanomagnetic composite perovskite	5 M KOH	5	730.04	16665.69	2159.88	this study

decreased from 2159.88 to 728.22 F/g (Figure 6d). For pure $BiFeO_3$, the maximum value for C_s was found to be around 649.50 F/g at 5 A/g (Figure S2). This further demonstrates how effective the method of introducing heterogeneous ions to materials is for enhancing their electrical properties. The electrochemical performance of the MBFO-NC nanocomposite is better than that of the reported electrode materials, as shown in Table 1.

Figure 7a displays the EIS results represented by Nyquist plots for the prepared MBFO-NC electrode. The plot was obtained in a semicircle with an alternating current frequency range from 10 Hz to 0.1 MHz and an amplitude of 5 mV. A semicircle and a straight line are used to illustrate the Warburg impedance (Z_w) and the charge transfer resistance (R_{ct}) at the electrode−electrolyte interface.[22b,38] The EIS equivalent circuit model can be seen in Figure 7a. There is a series of resistance included in the circuit: R_{ct}, the electrochemical system's solution resistance (R_s), Z_w, and a double-layer capacitor (C_{dl}). For MBFO-NC, the R_s and R_{ct} values are 13 and 21 Ω, respectively. Furthermore, these values line up with MBFO-

https://doi.org/10.1021/acsomega.3c00259
ACS Omega 2023, 8, 16145−16157

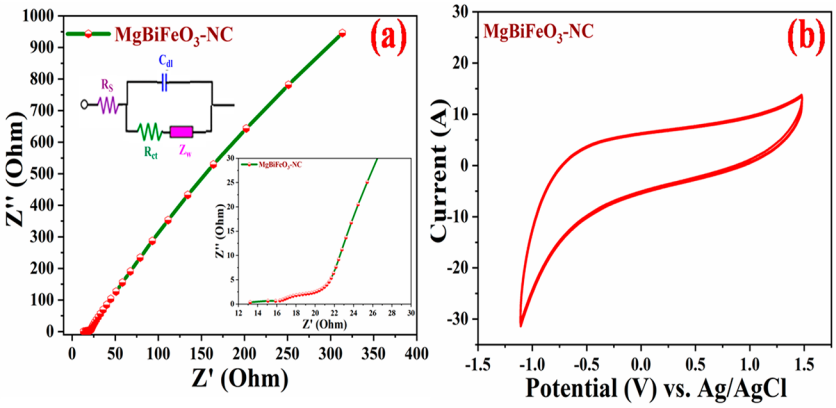

Figure 7. (a) EIS study of the MBFO-NC nanomagnetic composite and (b) CV cyclic stability.

NC's high ionic conductivity, which denotes the high stability of the prepared electrode.[39] According to our findings, the porous MBFO-NC nanomagnetic composite exhibits excellent electrochemical performance for supercapacitors. This enhancement is attributed to the pores in the carbon lattice acting as electrolyte ion reservoirs. These reservoirs ensure the quick and consistent transport of electrolyte ions.[40] The nitrogen-doped carbon in the MBFO-NC nanomagnetic composite demonstrates considerably better electrochemical performance compared to pure metal oxides because of its conducting nature, redox activity, and high surface area. Symmetric GCD curves of the MBFO-NC nanomagnetic composite exhibit high Coulombic indicators of the electrochemical process and excellent reversibility. The MBFO-NC electrode has remarkable cyclic stability over 20 000 segments at 50 mV/s, as shown in (Figure 7b).

Using the two-electrode testing system, the following eqs 9−11 are used to determine the specific capacitance (C_t, F/g), energy density (E_t, Wh/kg), and power density (P_t, W/kg) of the symmetric electrode:

$$C_t = \frac{4I \times \Delta t}{m \times \Delta V}\ \mathrm{F/g} \tag{9}$$

$$E_t = \frac{1}{8 \times 3.6} C_t \Delta V^2\ \mathrm{Wh/kg} \tag{10}$$

$$P_t = \frac{E_t}{\Delta t} \times 3600\ \mathrm{W/kg} \tag{11}$$

Figure 8 shows the Ragone plot to demonstrate the entire capability of the MBFO-NC nanomagnetic composite. At a power density of 5284.83 W/kg, the symmetric cell showed the highest energy density of about 730.04 Wh/kg. In contrast, at a power density of 16665.69 W/kg the energy density decreased to 227.57 Wh/kg. Therefore, the MBFO-NC nanomagnetic composite demonstrates superior power density and excellent energy density, which are crucial for being environmentally friendly and commercially viable.[41] Various factors contributed to the outstanding performance of the MBFO-NC symmetric electrode material, including the nitrogen-doped carbon lattice, charge transfer resistance, reduced ionic diffusion, and enhanced wettability of carbon materials in electrolyte solutions. The nitrogen-doped carbon lattice can enhance the electronic conductivity and specific capacitance. Additionally, the presence of magnesium ions increases the electronic density of the electrolyte.[22b] Additionally, the reduced internal

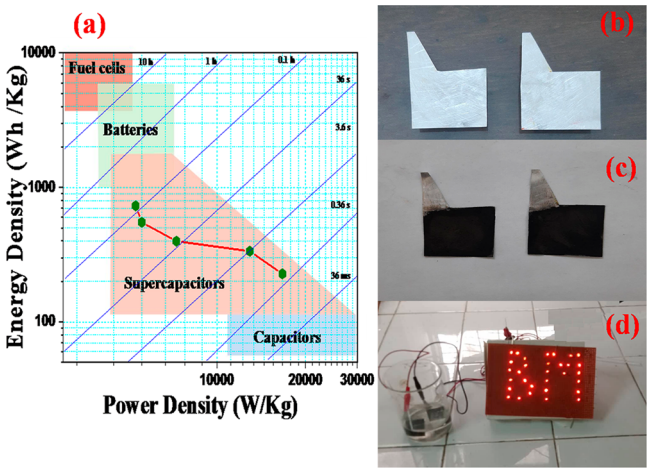

Figure 8. (a) Ragone plot of the MBFO-NC // MBFO-NC symmetric cell, (b) image of the aluminum substrate before MBFO-NC coating, (c) image of the aluminum substrate after MBFO-NC coating, (d) and practical clear application of the electrode material to light the laboratory panel, which contained 31 LEDs.

resistance of the MBFO-NC electrode also enables a quicker rate of charge transport between the active substance and the electrolyte. Furthermore, the EDLC characteristics of MBFO-NC also expedite the charge transfer when used with a highly ion-conductive aqueous electrolyte. Due to the higher electroactive surface of MBFO-NC, a fast and transient faradic reaction occurs. As a result, these nanomaterials could provide a short electrolyte transportation route.[37,42] The symmetric MBFO-NC//MBFO-NC supercapacitor cell was fabricated, and two "L" shaped aluminum substrates were coated with nanocomposite-based MBFO-NC as electrodes. Digital images of the aluminum substrate after and before MBFO-NC coating are shown in Figure 8b and c, respectively. One of these electrodes was labeled as the positive electrode, while the other was marked as the negative electrode. In the next step, these two substrates were kept in a beaker containing 5.0 M KOH. The manufactured MBFO-NC//MBFO-NC replica electrodes were connected to a laboratory plate (BM), whereby the MBFO-NC//MBFO-NC replica electrode was used for a practical application of the electrode material for the illumination of the BM, which contains 31 LEDs as shown in Figure 8 d. This shows how crucial the use of the manufactured symmetric cell electrodes MBFO-NC//MBFO-NC is in portable electronic devices for daily use.[43]

https://doi.org/10.1021/acsomega.3c00259
ACS Omega 2023, 8, 16145−16157

CONCLUSION

A mesoporous nitrogen-doped carbon $MgBiFeO_3$ nanomagnetic perovskite with a size of around 15 nm was fabricated using the polymeric method at 800 °C for 6 h in inert gas. BET analysis showed the MBFO-NC nanomagnetic perovskite has an excellent specific surface area of 415 m^2/ g. The crystal structure, elemental surface, and morphology of the MBFO-NC nanomagnetic perovskite were investigated using XRD, XPS, FTIR, FESEM, and HRTEM techniques. H_2-TPR analysis confirmed the doping of Mg^{2+} reduced the number of oxygen vacancies in the MBFO-NC nanomagnetic composites. The synthesized MBFO-NC nanomagnetic perovskite exhibits ferromagnetic properties with a saturation magnetization value of around 17.91 emu/g. The ultimate goal of supercapacitor technical development is to achieve better energy densities while keeping high power densities in order to introduce these devices for practical applications. This can only be done through concerted efforts incorporating the timely advancement of numerous components, such as electrodes, electrolytes, and separators. The supercapacitor produced by MBFO-NC as the electrode material in 5 M KOH electrolyte showed an enhanced C_s of 2079.44 F/g at 30 mV/s. Furthermore, GCD studies exhibit better improved capacitive performance at 5 A/g current density with a C_s of 2159.88 F/g. The MBFO-NC nanomagnetic composite showed a specific capacitance enhanced by 3.4× compared to that of the pure $BiFeO_3$ sample. Interestingly, at a power density of 5284.83 W/kg, the symmetric cell showed the highest energy density of about 730.04 Wh/kg. In contrast, at a power density of 16665.69 W/kg, the energy density decreased to 227.57 Wh/kg. The MBFO-NC electrode has remarkable cyclic stability over 20 000 cycles at 50 mV/s with an excellent retention capacity. The excellent C_s of the MBFO-NC nanomagnetic perovskite electrode can be attributed to porosity, which provides many active sites for redox mechanisms, high surface area, and interconnected mesoporous networks that facilitate the easy transportation of electrolyte ions and quick kinetic reaction. Additionally, nitrogen-doped graphitic carbon has a synergistic effect that improves electron transport while increasing conductivity. To build a superior electrode nanocomposite for energy storage, the lab panel which has 31 LEDs was illuminated as a practical use of the electrode material. This shows how crucial it is to employ MBFO-NC//MBFO-NC replica cell electrodes in portable electronics for daily use.

ASSOCIATED CONTENT

Supporting Information

The Supporting Information is available free of charge at https://pubs.acs.org/doi/10.1021/acsomega.3c00259.

Electrochemical properties of $BiFeO_3$ and the H_2-TPR of BFO-NC and MBFO-NC perovskites (PDF)

AUTHOR INFORMATION

Corresponding Authors

Basheer Mohammed Al-Maswari − *Department of Chemistry, Yuvaraja's College, University of Mysore, Mysuru, Karnataka 570005, India;* orcid.org/0000-0002-2503-208X; Email: basheer.almaswari@gmail.com

Bellale Marigowda Venkatesha − *Department of Chemistry, Yuvaraja's College, University of Mysore, Mysuru, Karnataka 570005, India*; Email: bmvenkatesha123@gmail.com

Authors

Nabil Al-Zaqri − *Department of Chemistry, College of Science, King Saud University, Riyadh 11451, Saudi Arabia*

Khaled Alkanad − *Department of Studies in Physics, University of Mysore, Mysuru, Karnataka 570006, India;* orcid.org/0000-0001-7746-3108

Fares Hezam AlOstoot − *Department of Chemistry, Yuvaraja's College, University of Mysore, Mysuru, Karnataka 570005, India*

Ahmed Boshaala − *Research Centre, Manchester Salt & Catalysis, Manchester University, Manchester M15 4AN, United Kingdom; Libyan Authority for Scientific Research, Tripoli, Libya*

Rayapura Thimmegowda Radhika − *Department of Chemistry, Maharani's Science College for Women, University of Mysore, Mysuru, Karnataka 570005, India*

Complete contact information is available at: https://pubs.acs.org/10.1021/acsomega.3c00259

Notes

The authors declare no competing financial interest.

ACKNOWLEDGMENTS

Basheer M. Almaswari is thankful to the University of Mysore, Mysore, India. All the authors are grateful to SAIF, IIT Bombay, and IIT Roorkee for carrying out the characterization of the research paper. The authors extend their appreciation to the Researchers Supporting Project number (RSP2023R396), King Saud University, Riyadh, Saudi Arabia.

REFERENCES

(1) Maksoud, M. A.; Fahim, R. A.; Shalan, A. E.; Abd Elkodous, M.; Olojede, S.; Osman, A. I.; Farrell, C.; Ala'a, H.; Awed, A.; Ashour, A.; et al. Advanced materials and technologies for supercapacitors used in energy conversion and storage: a review. *Environmental Chemistry Letters* **2021**, *19*, 375−439.

(2) (a) Hezam, A.; Alkanad, K.; Bajiri, M. A.; Strunk, J.; Takahashi, K.; Drmosh, Q. A.; Al-Zaqri, N.; Krishnappagowda, L. N. 2D/1D MoS_2/TiO_2 heterostructure photocatalyst with a switchable CO_2 reduction product. *Small Methods* **2023**, *7* (1), 2201103. (b) Alkanad, K.; Hezam, A.; Al-Zaqri, N.; Bajiri, M. A.; Alnaggar, G.; Drmosh, Q. A.; Almukhlifi, H. A.; Neratur Krishnappagowda, L. One-Step Hydrothermal Synthesis of Anatase TiO_2 Nanotubes for Efficient Photocatalytic CO_2 Reduction. *ACS omega* **2022**, *7* (43), 38686−38699. (c) Oloore, L. E.; Gondal, M. A.; Popoola, A.; Popoola, I. K. Pseudocapacitive contributions to enhanced electrochemical energy storage in hybrid perovskite-nickel oxide nanoparticles composites electrodes. *Electrochim. Acta* **2020**, *361*, 137082.

(3) Ghosh, A.; Trujillo, D. P.; Choi, H.; Nakhmanson, S.; Alpay, S. P.; Zhu, J.-X. Electronic and magnetic properties of lanthanum and strontium doped bismuth ferrite: a first-principles study. *Sci. Rep.* **2019**, *9*, 194.

(4) Zhou, D.; Guan, Y.; Vopson, M. M.; Xu, J.; Liang, H.; Cao, F.; Dong, X.; Mueller, J.; Schenk, T.; Schroeder, U. Electric field and temperature scaling of polarization reversal in silicon doped hafnium oxide ferroelectric thin films. *Acta Mater.* **2015**, *99*, 240−246.

(5) Hoffmann, M.; Schroeder, U.; Künneth, C.; Kersch, A.; Starschich, S.; Böttger, U.; Mikolajick, T. Ferroelectric phase transitions in nanoscale HfO_2 films enable giant pyroelectric energy conversion and highly efficient supercapacitors. *Nano Energy* **2015**, *18*, 154−164.

(6) (a) Goncalves, L.; Rocha, L.; Longo, E.; Simões, A. Calcium doped $BiFeO_3$ films: Rietveld analysis and piezoelectric properties. *Journal of Materials Science: Materials in Electronics* **2018**, *29* (1), 784−793. (b) Chakraborty, R.; Mukherjee, S.; Mukherjee, S. Effect of zinc

doping on phase evolution and characterization of nanocrystalline bismuth ferrite synthesized by chemical solution route. *Journal of the Australian Ceramic Society* **2017**, *53* (1), 57−65.

(7) (a) Tabari, T.; Singh, D.; Calisan, A.; Ebadi, M.; Tavakkoli, H.; Caglar, B. Microwave assisted synthesis of $La_{1-x}Ca_xMnO_3$ (x= 0, 0.2 and 0.4): Structural and capacitance properties. *Ceram. Int.* **2017**, *43* (17), 15970−15977. (b) Mefford, J. T.; Hardin, W. G.; Dai, S.; Johnston, K. P.; Stevenson, K. J. Anion charge storage through oxygen intercalation in $LaMnO_3$ perovskite pseudocapacitor electrodes. *Nature materials* **2014**, *13* (7), 726−732. (c) Cao, Y.; Lin, B.; Sun, Y.; Yang, H.; Zhang, X. Symmetric/Asymmetric Supercapacitor Based on the Perovskite-type Lanthanum Cobaltate Nanofibers with Sr-substitution. *Electrochim. Acta* **2015**, *178*, 398−406. (d) Lang, X.; Mo, H.; Hu, X.; Tian, H. Supercapacitor performance of perovskite $La_{1-x}Sr_xMnO_3$. *Dalton transactions* **2017**, *46* (40), 13720−13730.

(8) Ma, Z.; Liu, H.; Wang, L.; Zhang, F.; Zhu, L.; Fan, S. Phase transition and multiferroic properties of Zr-doped $BiFeO_3$ thin films. *Journal of Materials Chemistry C* **2020**, *8* (48), 17307−17317.

(9) Surdu, V.-A.; Truşcă, R. D.; Vasile, B. Ş.; Oprea, O. C.; Tanasă, E.; Diamandescu, L.; Andronescu, E.; Ianculescu, A. C. $Bi_{1-x}Eu_xFeO_3$ Powders: Synthesis, Characterization, Magnetic and Photoluminescence Properties. *Nanomaterials* **2019**, *9* (10), 1465.

(10) (a) Aziz, S. B.; Brza, M.; Hamsan, M.; Kadir, M.; Muzakir, S.; Abdulwahid, R. T. Effect of ohmic-drop on electrochemical performance of EDLC fabricated from PVA: dextran: NH4I based polymer blend electrolytes. *Journal of Materials Research and Technology* **2020**, *9* (3), 3734−3745. (b) Feng, Y.; Chen, S.; Wang, J.; Lu, B. Carbon foam with microporous structure for high performance symmetric potassium dual-ion capacitor. *Journal of Energy Chemistry* **2020**, *43*, 129−138.

(11) Kiamahalleh, M. V.; Zein, S. H. S.; Najafpour, G.; SATA, S. A.; Buniran, S. Multiwalled carbon nanotubes based nanocomposites for supercapacitors: a review of electrode materials. *Nano* **2012**, *07* (02), 1230002.

(12) (a) Inagaki, M.; Konno, H.; Tanaike, O. Carbon materials for electrochemical capacitors. *J. Power Sources* **2010**, *195* (24), 7880−7903. (b) Zhang, D.; Zhang, X.; Chen, Y.; Yu, P.; Wang, C.; Ma, Y. Enhanced capacitance and rate capability of graphene/polypyrrole composite as electrode material for supercapacitors. *J. Power Sources* **2011**, *196* (14), 5990−5996.

(13) (a) Chandrasekaran, S.; Zhang, C.; Shu, Y.; Wang, H.; Chen, S.; Edison, T. N. J. I.; Liu, Y.; Karthik, N.; Misra, R.; Deng, L.; et al. Advanced opportunities and insights on the influence of nitrogen incorporation on the physico-/electro-chemical properties of robust electrocatalysts for electrocatalytic energy conversion. *Coord. Chem. Rev.* **2021**, *449*, 214209. (b) Chen, M.; Li, H.; Liu, C.; Liu, J.; Feng, Y.; Wee, A. G.; Zhang, B. Porphyrin-and porphyrinoid-based covalent organic frameworks (COFs): From design, synthesis to applications. *Coord. Chem. Rev.* **2021**, *435*, 213778. (c) Yu, D.; Ma, Y.; Hu, F.; Lin, C. C.; Li, L.; Chen, H. Y.; Han, X.; Peng, S. Dual-Sites Coordination Engineering of Single Atom Catalysts for Flexible Metal−Air Batteries. *Adv. Energy Mater.* **2021**, *11* (30), 2101242.

(14) (a) He, J.; Li, N.; Li, Z. G.; Zhong, M.; Fu, Z. X.; Liu, M.; Yin, J. C.; Shen, Z.; Li, W.; Zhang, J.; et al. Strategic Defect Engineering of Metal−Organic Frameworks for Optimizing the Fabrication of Single-Atom Catalysts. *Adv. Funct. Mater.* **2021**, *31* (41), 2103597. (b) Liu, X.; Ye, S.; Lan, G.; Su, P.; Zhang, X.; Price, C. A. H.; Li, Y.; Liu, J. Atomic Pyridinic Nitrogen Sites Promoting Levulinic Acid Hydrogenations over Double-Shelled Hollow Ru/C Nanoreactors. *Small* **2021**, *17* (33), 2101271. (c) Jiao, L.; Ye, W.; Kang, Y.; Zhang, Y.; Xu, W.; Wu, Y.; Gu, W.; Song, W.; Xiong, Y.; Zhu, C. Atomically dispersed N-coordinated Fe-Fe dual-sites with enhanced enzyme-like activities. *Nano Research* **2022**, *15* (2), 959−964. (d) Choi, S.; Kwon, J.; Jo, S.; Kim, S.; Park, K.; Kim, S.; Han, H.; Paik, U.; Song, T. Highly efficient and stable bifunctional electrocatalysts with decoupled active sites for hydrogen evolution and oxygen reduction reactions. *Applied Catalysis B: Environmental* **2021**, *298*, 120530.

(15) (a) Li, X.; Hou, K.; Qiu, D.; Yi, P.; Lai, X. A first principles and experimental study on the influence of nitrogen doping on the performance of amorphous carbon films for proton exchange membrane fuel cells. *Carbon* **2020**, *167*, 219−229. (b) Chaban, V. V.; Andreeva, N. A. Structure, thermodynamic and electronic properties of carbon-nitrogen cubanes and protonated polynitrogen cations. *J. Mol. Struct.* **2017**, *1149*, 828−834.

(16) (a) Chaban, V. V.; Prezhdo, O. V. Nitrogen−nitrogen bonds undermine stability of N-doped graphene. *J. Am. Chem. Soc.* **2015**, *137* (36), 11688−11694. (b) Naushad, M.; Ahamad, T.; Al-Maswari, B. M.; Alqadami, A. A.; Alshehri, S. M. Nickel ferrite bearing nitrogen-doped mesoporous carbon as efficient adsorbent for the removal of highly toxic metal ion from aqueous medium. *Chemical Engineering Journal* **2017**, *330*, 1351−1360. (c) Al-Maswari, B. M.; Ahmed, J.; Alzaqri, N.; Ahamad, T.; Mao, Y.; Hezam, A.; Venkatesha, B. Synthesis of perovskite bismuth ferrite embedded nitrogen-doped Carbon ($BiFeO_3$-NC) nanocomposite for energy storage application. *Journal of Energy Storage* **2021**, *44*, 103515.

(17) Čebela, M.; Janković, B. Ž.; Hercigonja, R. V.; Lukić, M. J.; Dohčević-Mitrović, Z.; Milivojević, D.; Matović, B. Comprehensive characterization of $BiFeO_3$ powder synthesized by the hydrothermal procedure. *Processing and Application of Ceramics* **2016**, *10* (4), 201−208.

(18) Shi, M.; Xin, Y.; Chen, X.; Zou, K.; Jing, W.; Sun, J.; Chen, Y.; Liu, Y. Coal-derived porous activated carbon with ultrahigh specific surface area and excellent electrochemical performance for supercapacitors. *J. Alloys Compd.* **2021**, *859*, 157856.

(19) (a) Dhawa, T.; Chattopadhyay, S.; De, G.; Mahanty, S. In situ mg/MgO-embedded mesoporous carbon derived from magnesium 1, 4-benzenedicarboxylate metal organic framework as sustainable Li−S battery cathode support. *ACS omega* **2017**, *2* (10), 6481−6491. (b) Basith, M.; Ahsan, R.; Zarin, I.; Jalil, M. Enhanced photocatalytic dye degradation and hydrogen production ability of $Bi_{25}FeO_{40}$-rGO nanocomposite and mechanism insight. *Sci. Rep.* **2018**, *8*, 11090.

(20) (a) Kossar, S.; Amiruddin, R.; Rasool, A. Study on thickness-dependence characteristics of bismuth ferrite (BFO) for ultraviolet (UV) photodetector application. *Micro and Nano Syst. Lett.* **2021**, *9*, 1. (b) Čebela, M.; Janković, B. Ž.; Hercigonja, R. V.; Lukic, M. J.; Dohcevic-Mitrovic, Z.; Milivojević, D.; Matović, B. Comprehensive characterization of $BiFeO_3$ powder synthesized by the hydrothermal procedure. *Processing and Application of Ceramics* **2016**, *10* (4), 201−208. (c) Shi, X.; Quan, S.; Yang, L.; Liu, C.; Shi, F. Anchoring Co_3O_4 on $BiFeO_3$: achieving high photocatalytic reduction in Cr (VI) and low cobalt leaching. *J. Mater. Sci.* **2019**, *54* (19), 12424−12436. (d) Durgalakshmi, D.; Ajay Rakkesh, R.; Kamil, S.; Karthikeyan, S.; Balakumar, S. Rapid Dilapidation of Alcohol Using Magnesium Oxide and Magnesium Aspartate based Nanostructures: A Raman Spectroscopic and Molecular Simulation Approach. *Journal of inorganic and Organometallic Polymers and Materials* **2019**, *29* (4), 1390−1399.

(21) Bajpai, O. P.; Mandal, S.; Ananthakrishnan, R.; Mandal, P.; Khastgir, D.; Chattopadhyay, S. Structural features, magnetic properties and photocatalytic activity of bismuth ferrite nanoparticles grafted on graphene nanosheets. *New J. Chem.* **2018**, *42* (13), 10712−10723.

(22) (a) Ghahfarokhi, S. M.; Shobegar, E. M. An investigation of the ethylene glycol surfactant on the structural, microstructure, magnetic and optical properties of $SrFe_2O_4$ nanoparticles. *J. Magn. Magn. Mater.* **2020**, *495*, 165866. (b) Al-Maswari, B. M.; Al-Zaqri, N.; Ahmed, J.; Ahamad, T.; Boshaala, A.; Ananda, S.; Venkatesha, B. Nanomagnetic strontium ferrite nitrogen doped carbon ($SrFe_2O_4$-NC): Synthesis, characterization and excellent supercapacitor performance. *Journal of Energy Storage* **2022**, *52*, 104821.

(23) Abdellahi, M.; Tajally, M.; Mirzaee, O. The effect of the particle size on the heating and drug release potential of the magnetic nanoparticles in a novel point of view. *J. Magn. Magn. Mater.* **2021**, *530*, 167938.

(24) (a) Anand, P.; Jaihindh, D. P.; Chang, W.-K.; Fu, Y.-P. Tailoring the Ca-doped bismuth ferrite for electrochemical oxygen evolution reaction and photocatalytic activity. *Appl. Surf. Sci.* **2021**, *540*, 148387. (b) Ma, C.-J.; Chen, Y.; Zhu, C.; Chen, Q.; Song, W.-L.;

https://doi.org/10.1021/acsomega.3c00259
ACS Omega 2023, 8, 16145−16157

Jiao, S.; Chen, H.; Fang, D. Bismuth ferrite: an abnormal perovskite with electrochemical extraction of ions from A site. *Journal of Materials Chemistry A* **2019**, *7* (19), 12176−12190.

(25) Alkanad, K.; Hezam, A.; Shekar, G. S.; Drmosh, Q.; Kala, A. A.; AL-Gunaid, M. Q.; Lokanath, N. Magnetic recyclable α-Fe_2O_3−Fe_3O_4/Co_3O_4−CoO nanocomposite with a dual Z-scheme charge transfer pathway for quick photo-Fenton degradation of organic pollutants. *Catalysis Science & Technology* **2021**, *11* (9), 3084−3097.

(26) (a) Yan, Z.; Gao, J.; Li, Y.; Zhang, M.; Guo, M. Hydrothermal synthesis and structure evolution of metal-doped magnesium ferrite from saprolite laterite. *RSC Adv.* **2015**, *5* (112), 92778−92787. (b) Guijarro, N.; Bornoz, P.; Prévot, M.; Yu, X.; Zhu, X.; Johnson, M.; Jeanbourquin, X.; Le Formal, F.; Sivula, K. Evaluating spinel ferrites MFe_2O_4 (M= Cu, Mg, Zn) as photoanodes for solar water oxidation: prospects and limitations. *Sustainable Energy & Fuels* **2018**, *2* (1), 103−117.

(27) Chen, J. L.; Zhu, J. H. A query on the Mg2p binding energy of MgO. *Res. Chem. Intermed.* **2019**, *45* (3), 947−950.

(28) (a) Remya, K.; Prabhu, D.; Joseyphus, R. J.; Bose, A. C.; Viswanathan, C.; Ponpandian, N. Tailoring the morphology and size of perovskite $BiFeO_3$ nanostructures for enhanced magnetic and electrical properties. *Materials & Design* **2020**, *192*, 108694. (b) Ali, S. E. Influence of preparation method on phase formation, structural and magnetic properties of $BiFeO_3$. *Journal of Electroceramics* **2022**, *48*, 95−101.

(29) (a) Jalil, M.; Chowdhury, S. S.; Alam Sakib, M.; Enamul Hoque Yousuf, S.; Khan Ashik, E.; Firoz, S. H.; Basith, M. Temperature-dependent phase transition and comparative investigation on enhanced magnetic and optical properties between sillenite and perovskite bismuth ferrite-rGO nanocomposites. *J. Appl. Phys.* **2017**, *122* (8), 084902. (b) Ma, C.-J.; Li, N.; Song, W.-L. Tailoring the electrochemical behaviors of bismuth ferrite using Ca ion doping. *Frontiers in Materials* **2020**, *7*, 15.

(30) Sasmal, A.; Sen, S.; Devi, P. S. Role of suppressed oxygen vacancies in the $BiFeO_3$ nanofiller to improve the polar phase and multifunctional performance of poly (vinylidene fluoride). *Phys. Chem. Chem. Phys.* **2019**, *21* (11), 5974−5988.

(31) (a) Ouyang, W.; Zeng, D.; Yu, X.; Xie, F.; Zhang, W.; Chen, J.; Yan, J.; Xie, F.; Wang, L.; Meng, H.; et al. Exploring the active sites of nitrogen-doped graphene as catalysts for the oxygen reduction reaction. *Int. J. Hydrogen Energy* **2014**, *39* (28), 15996−16005. (b) Ariharan, A.; Viswanathan, B.; Nandhakumar, V. Nitrogen doped graphene as potential material for hydrogen storage. *Graphene* **2017**, *6* (2), 41−60. (c) Ahamad, T.; Naushad, M.; Al-Saeedi, S. I.; Alshehri, S. M. N/S-doped carbon embedded with AgNPs as a highly efficient catalyst for the reduction of toxic organic pollutants. *Mater. Lett.* **2020**, *264*, 127310. (d) Huang, Y.; Yan, H.; Zhang, C.; Wang, Y.; Wei, Q.; Zhang, R. Interfacial Electronic Effects in Co@ N-Doped Carbon Shells Heterojunction Catalyst for Semi-Hydrogenation of Phenylacetylene. *Nanomaterials* **2021**, *11* (11), 2776.

(32) Costa, L.; Deus, R.; Foschini, C.; Longo, E.; Cilense, M.; Simões, A. Experimental evidence of enhanced ferroelectricity in Ca doped $BiFeO_3$. *Mater. Chem. Phys.* **2014**, *144* (3), 476−483.

(33) He, J.; Guo, R.; Fang, L.; Dong, W.; Zheng, F.; Shen, M. Characterization and visible light photocatalytic mechanism of size-controlled $BiFeO_3$ nanoparticles. *Mater. Res. Bull.* **2013**, *48* (9), 3017−3024.

(34) Wu, S.; Zhang, J.; Liu, X.; Lv, S.; Gao, R.; Cai, W.; Wang, F.; Fu, C. Micro-area ferroelectric, piezoelectric and conductive properties of single $BiFeO_3$ nanowire by scanning probe microscopy. *Nanomaterials* **2019**, *9* (2), 190.

(35) Mo, H.; Nan, H.; Lang, X.; Liu, S.; Qiao, L.; Hu, X.; Tian, H. Influence of calcium doping on performance of $LaMnO_3$ supercapacitors. *Ceram. Int.* **2018**, *44* (8), 9733−9741.

(36) (a) GC, S. S.; Alkanad, K.; B, T.; Alnaggar, G.; Al Zaqri, N.; Drmosh, Q.A.; Boshaala, A.; NK, L. Alkaline mediated sono-synthesis of surface oxygen-vacancies-rich cerium oxide for efficient photocatalytic CO_2 reduction to methanol. *Surf. Interfaces* **2022**, *34*, 102389. (b) Xie, Y.; Zhang, C.; Wang, D.; Lu, J.; Wang, Y.; Wang, J.; Zhang, L.; Zhang, R. Catalytic performance of a Bi_2O_3−Fe_2O_3 system in soot combustion. *New J. Chem.* **2019**, *43* (38), 15368−15374.

(37) Ghadimi, L. S.; Arsalani, N.; Tabrizi, A. G.; Mohammadi, A.; Ahadzadeh, I. Novel nanocomposite of $MnFe_2O_4$ and nitrogen-doped carbon from polyaniline carbonization as electrode material for symmetric ultra-stable supercapacitor. *Electrochim. Acta* **2018**, *282*, 116−127.

(38) Barai, H. R.; Rahman, M. M.; Joo, S. W. Template-free synthesis of two-dimensional titania/titanate nanosheets as electrodes for high-performance supercapacitor applications. *J. Power Sources* **2017**, *372*, 227−234.

(39) Maier, M.; Suresh Babu, R.; Sampaio, D.; de Barros, A. Binder-free polyaniline interconnected metal hexacyanoferrates nanocomposites (Metal= Ni, Co) on carbon fibers for flexible supercapacitors. *Journal of Materials Science: Materials in Electronics* **2017**, *28* (23), 17405−17413.

(40) (a) Mehrez, J. A.-A.; Owusu, K. A.; Chen, Q.; Li, L.; Hamwi, K.; Luo, W.; Mai, L. Hierarchical $MnCo_2O_4$@ $NiMoO_4$ as free-standing core−shell nanowire arrays with synergistic effect for enhanced supercapacitor performance. *Inorganic Chemistry Frontiers* **2019**, *6* (3), 857−865. (b) Ubaidullah, M.; Ahmed, J.; Ahamad, T.; Shaikh, S. F.; Alshehri, S. M.; Al-Enizi, A. M. Hydrothermal synthesis of novel nickel oxide@ nitrogenous mesoporous carbon nanocomposite using costless smoked cigarette filter for high performance supercapacitor. *Mater. Lett.* **2020**, *266*, 127492.

(41) Venkateswarlu, S.; Mahajan, H.; Panda, A.; Lee, J.; Govindaraju, S.; Yun, K.; Yoon, M. Fe3O4 nano assembly embedded in 2D-crumpled porous carbon sheets for high energy density supercapacitor. *Chemical Engineering Journal* **2021**, *420*, 127584.

(42) (a) Kumar, A.; Kumar, N.; Sharma, Y.; Leu, J.; Tseng, T. Y. Synthesis of free-standing flexible rGO/MWCNT films for symmetric supercapacitor application. *Nanoscale Res. Lett.* **2019**, *14*, 266. (b) Yang, H.; Kannappan, S.; Pandian, A. S.; Jang, J.-H.; Lee, Y. S.; Lu, W. Graphene supercapacitor with both high power and energy density. *Nanotechnology* **2017**, *28* (44), 445401. (c) Sharifi, S.; Yazdani, A.; Rahimi, K. Incremental substitution of Ni with Mn in $NiFe_2O_4$ to largely enhance its supercapacitance properties. *Sci. Rep.* **2020**, *10*, 10916.

(43) Raut, S. D.; Shinde, N. M.; Ghule, B. G.; Kim, S.; Pak, J. J.; Xia, Q.; Mane, R. S. Room-temperature solution-processed sharp-edged nanoshapes of molybdenum oxide for supercapacitor and electrocatalysis applications. *Chemical Engineering Journal* **2022**, *433*, 133627.

(44) Tabrizi, A. G.; Arsalani, N.; Mohammadi, A.; Namazi, H.; Ghadimi, L. S.; Ahadzadeh, I. Facile synthesis of a $MnFe_2O_4$/rGO nanocomposite for an ultra-stable symmetric supercapacitor. *New J. Chem.* **2017**, *41* (12), 4974−4984.

(45) Wongpratat, U.; Tipsawat, P.; Khajonrit, J.; Swatsitang, E.; Maensiri, S. Effects of nickel and magnesium on electrochemical performances of partial substitution in spinel ferrite. *J. Alloys Compd.* **2020**, *831*, 154718.

(46) Sarkar, A.; Singh, A. K.; Sarkar, D.; Khan, G. G.; Mandal, K. Three-dimensional nanoarchitecture of $BiFeO_3$ anchored TiO_2 nanotube arrays for electrochemical energy storage and solar energy conversion. *ACS Sustainable Chem. Eng.* **2015**, *3* (9), 2254−2263.

(47) Uke, S. J.; Mardikar, S. P.; Bambole, D. R.; Kumar, Y.; Chaudhari, G. N. Sol-gel citrate synthesized Zn doped $MgFe_2O_4$ nanocrystals: a promising supercapacitor electrode material. *Materials Science for Energy Technologies* **2020**, *3*, 446−455.

(48) Cai, Y.-Z.; Cao, W.-Q.; Zhang, Y.-L.; He, P.; Shu, J.-C.; Cao, M.-S. Tailoring rGO-$NiFe_2O_4$ hybrids to tune transport of electrons and ions for supercapacitor electrodes. *J. Alloys Compd.* **2019**, *811*, 152011.

(49) Kaipannan, S.; Govindarajan, K.; Sundaramoorthy, S.; Marappan, S. Waste toner-derived carbon/Fe_3O_4 nanocomposite for high-performance supercapacitor. *ACS omega* **2019**, *4* (14), 15798−15805.

(50) Mousa, M.; Khairy, M.; Shehab, M. Nanostructured ferrite/graphene/polyaniline using for supercapacitor to enhance the

capacitive behavior. *J. Solid State Electrochem.* **2017**, *21* (4), 995−1005.

(51) Khajonrit, J.; Wongpratat, U.; Kidkhunthod, P.; Pinitsoontorn, S.; Maensiri, S. Effects of Co doping on magnetic and electrochemical properties of $BiFeO_3$ nanoparticles. *J. Magn. Magn. Mater.* **2018**, *449*, 423−434.

(52) Khajonrit, J.; Phumying, S.; Maensiri, S. Structure and magnetic/electrochemical properties of Cu-doped $BiFeO_3$ nanoparticles prepared by a simple solution method. *Jpn. J. Appl. Phys.* **2016**, *55* (6S1), 06GJ14.

(53) Kitchamsetti, N.; Samtham, M.; Didwal, P. N.; Kumar, D.; Singh, D.; Bimli, S.; Chikate, P. R.; Basha, D. A.; Kumar, S.; Park, C.-J.; et al. Theory abide experimental investigations on morphology driven enhancement of electrochemical energy storage performance for manganese titanate perovskites electrodes. *J. Power Sources* **2022**, *538*, 231525.

(54) Moitra, D.; Anand, C.; Ghosh, B. K.; Chandel, M.; Ghosh, N. N. One-dimensional $BiFeO_3$ nanowire-reduced graphene oxide nanocomposite as excellent supercapacitor electrode material. *ACS Applied Energy Materials* **2018**, *1* (2), 464−474.

(55) Naushad, M.; Ahamad, T.; Ubaidullah, M.; Ahmed, J.; Ghafar, A. A.; Al-Sheetan, K. M.; Arunachalam, P. Nitrogen-doped carbon quantum dots (N-CQDs)/Co_3O_4 nanocomposite for high performance supercapacitor. *Journal of King Saud University-Science* **2021**, *33* (1), 101252.

https://doi.org/10.1021/acsomega.3c00259
ACS Omega 2023, 8, 16145−16157